

Broadband Brillouin Phase Shifter Utilizing RF Interference: Experimental Demonstration and Theoretical Analysis

Luke McKay¹, Moritz Merklein¹, Amol Choudhary², Yang Liu¹, Micah Jenkins, Charles Middleton, Alex Cramer, Andrew Chilton, Joseph Devenport, Khu Vu, Duk-Yong Choi³, Pan Ma, Stephen J. Madden, Richard DeSalvo⁴, and Benjamin J. Eggleton¹

Abstract—Microwave photonic phase shifters based on stimulated Brillouin scattering (SBS) offer tunable and broadband, optically controllable phase shifts. However, achieving a 360° phase shift requires a large amount of SBS gain which often exceeds the available gain and power handling capability of an integrated waveguide. A Radio Frequency (RF) interference technique has recently been utilized in an integrated silicon platform, which uses forward Brillouin scattering in a suspended waveguide to compensate for the lack of available Brillouin gain in standard silicon on insulator platforms. This interference scheme amplifies the phase shift at the expense of link performance. Here, we demonstrate and analytically model a 360° ultra-broadband phase shifter using backward SBS in both fiber and on-chip by combining SBS and RF interference. The phase enhancement scheme greatly reduces the required Brillouin gain and thus the required optical power. Additionally, the backward architecture reduces filter requirements as the residual pump reflections are simpler to remove compared to the pump in the forward Brillouin scattering case, where the pump co-propagates with the signal. The model provides a deeper insight into the properties of the interferometric phase enhancement scheme and predicts the potential trade-offs of an optimized system, showing reduced link loss at higher levels of Brillouin gain. The model also predicts the sensitivity to variations

of the interferometric components. Using this technique, we have demonstrated a broadband phase shift over an ultra-broad bandwidth of 0.1–65 GHz, limited only by the bandwidth of the available components. Also, we demonstrate a phase enhancement factor of 10 over a bandwidth of 18 GHz in an integrated chalcogenide waveguide.

Index Terms—Integrated optics, integrated optics devices, nonlinear optics, radio frequency photonics, stimulated Brillouin scattering.

I. INTRODUCTION

MICROWAVE photonics (MWP) has great potential in the field of Radio Frequency (RF) phase shifters, offering far superior bandwidth, electromagnetic immunity and flexible operating frequency bands compared to electrical equivalents [1], [2]. Phase shifters are a fundamental component in the field of RF electronics and have a wide range of applications, particularly in Phased Array Antennas (PAA) [3]. Through controlling the phase to each identical antenna element in an array, the resultant beam profile can be dynamically steered. This significantly increases the utility when compared to static or mechanically controlled antennas. With constant improvements to performance, PAA's are becoming integral in many applications including areas such as satellite communication, RADAR, medical imaging and 5G, among others [3]–[5]. In a microwave photonics system, the RF signal is modulated upon an optical carrier, where an optical phase shift can be translated to an RF phase shift by acting on the carrier before photodetection. The ideal microwave-photonic phase shifter can induce a continuously tunable phase shift of 360° over broad bandwidths with minimal RF insertion loss, small amplitude deviations with low Size, Weight, and Power consumption (SWaP) characteristics.

There have been different methods demonstrated to induce a broadband phase shift using microwave photonics in fibers, such as fiber Bragg gratings [6], [7], frequency mixing [8], [9], polarization modulation [10] as well as Sagnac interferometry [11] and Brillouin scattering [12].

Integrating microwave photonic devices into a chip can provide significant benefits, particularly improvements in stability, scalability as well as a reduction in SWaP [1]. Despite the immense promise of integrated microwave photonics, integration comes with its own challenges, such as link performance [1],

Manuscript received October 2, 2019; revised January 26, 2020 and February 27, 2020; accepted March 6, 2020. Date of publication March 12, 2020; date of current version July 20, 2020. This work was supported in part by Australian Research Council (ARC) under Grant LP170100112, in part by U.S. Air Force (USAF) under Grant FA2386-16-1-4036, and in part by U.S. Office of Naval Research Global (ONRG) under Grant N62909-18-1-2013. (Corresponding author: Moritz Merklein.)

Luke McKay, Moritz Merklein, Yang Liu, and Benjamin J. Eggleton are with the University of Sydney Nano Institute (Sydney Nano), Institute of Photonics and Optical Science (IPOS), School of Physics, The University of Sydney, Sydney, NSW 2006, Australia (e-mail: lmck3273@uni.sydney.edu.au; moritz.merklein@sydney.edu.au; yang.liu@sydney.edu.au; benjamin.eggleton@sydney.edu.au).

Amol Choudhary is with the Department of Electrical Engineering, Indian Institute of Technology, Delhi 110016, India (e-mail: Amol.Choudhary@ee.iitd.ac.in).

Micah Jenkins, Charles Middleton, Alex Cramer, Andrew Chilton, Joseph Devenport, and Richard DeSalvo are with the L3Harris Technologies, Melbourne, FL 32919 USA (e-mail: Micah.Jenkins@L3Harris.com; Charles.Middleton@L3Harris.com; Alex.Cramer@L3Harris.com; Andy.chilton@L3harris.com; Joseph.Devenport@L3Harris.com; Richard.desalvo@l3harris.com).

Khu Vu, Duk-Yong Choi, Pan Ma, and Stephen J. Madden are with the Laser Physics Centre, The Australian National University, Canberra, ACT 0200, Australia (e-mail: khu.vu@anu.edu.au; duk.choi@anu.edu.au; pan.ma@anu.edu.au; stephen.madden@anu.edu.au).

Color versions of one or more of the figures in this article are available online at <http://ieeexplore.ieee.org>.

Digital Object Identifier 10.1109/JLT.2020.2980308

[13]. However, numerous approaches to realizing integrated microwave photonic phase shifters have been reported. For example, structures exploiting the resonant response of rings or gratings to induce the optical phase shift have been used [14]–[16]. The electro-optic effect has also been used in silicon P-N junctions to induce rapid and precise phase shifts, however, this comes at the expense of optical loss, and has poor spectral selectivity which limits device flexibility [17], [18]. A 360° phase shifter based on the electro-optical effect has been demonstrated with most components realized in an integrated form factor [19]. On the other hand, a phase shift can be induced with nonlinear optical effects such as Stimulated Brillouin scattering (SBS) [20]. SBS is able to induce a narrowband gain-based phase shift on an optical carrier, which is optically controllable [12], [21], [22]. Due to the spectrally narrow Brillouin response, it is possible to induce a phase shift on an optical signal without affecting those around it. This narrowband response enables the phase shifter to operate at low RF frequencies while simultaneously amplifying the signal. Brillouin scattering has been used to induce broadband gain-based phase shifts in both fibers and chips [12], [23], [24]. However, a large amount of Brillouin gain is required to achieve 360° phase shifts, limiting practical usage in chip-based devices due to gain limitations, power handling of the chip and power consumption. Recently, a Brillouin-based phase shifter was demonstrated in a silicon waveguide using only 1.6 dB of forward Brillouin gain, enabled by an interferometric broadband phase enhancement scheme over a bandwidth of 15 GHz [25]. Forward Brillouin scattering requires the optical pump to co-propagate with the probe. Due to the relatively large difference in the amplitude between these components, this presents a challenge to sufficiently filter out the pump before the photodetector, which can cause distortion. This difficulty in filtering the pump is compounded by the relatively small Brillouin frequency shift in silicon which is less than 4.5 GHz, so a high roll-off filter is required [25], [26].

In this work, we demonstrate a broadband RF phase shifter using backward SBS, implemented both in a chalcogenide chip and in fiber. Backward SBS is exploited, which relaxes the requirements of filtering the pump when compared to forward Brillouin scattering. This is because the optically encoded RF signal and the pump are counter-propagating, so only the relatively small pump back-reflections need to be removed to prevent unwanted beating at the photo-detector. A phase enhancement factor of approximately 10 was demonstrated and achieved a 360° phase shift in an integrated chalcogenide waveguide over a bandwidth of 18 GHz. 360° phase tunability was also demonstrated over an ultra-wide bandwidth of 65 GHz in fiber, which is practically limited only by the bandwidth of our modulator and photodetector and can in principle be extended much further. To explain and further explore the phase enhancement concept, an analytical model of the broadband interference scheme was developed. The analysis provides a model for the link trade-off with phase enhancement factor as well as link deviation over the Brillouin resonance. The model also provides an insight into the operation of the phase enhancement system when the amplitudes of the optical interferometric components are misaligned.

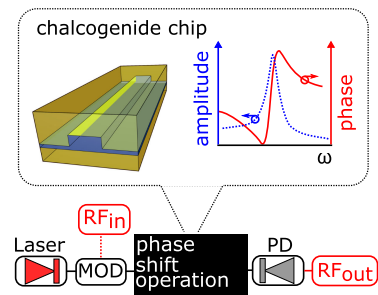


Fig. 1. Principle of the microwave photonic phase shifter. Bottom: A basic scheme of an MWP phase shifter. The RF input is modulated upon the optical carrier generating sidebands which later beat at the photodetector to generate an RF output. Top: A phase shift is induced on the optical carrier using SBS which results in a phase-shifted output RF signal. MOD, modulator; ω , frequency; $\text{RF}_{\text{in/out}}$, Radio Frequency signal input/output.

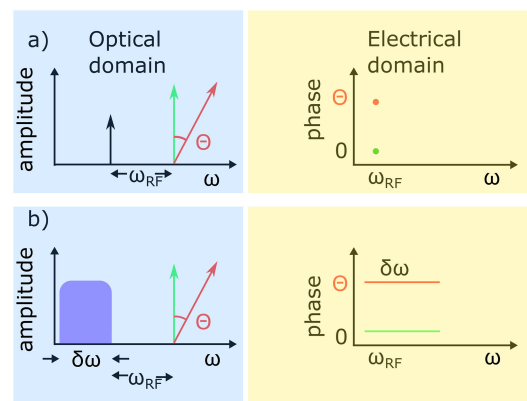


Fig. 2. (a) In the optical domain, two tones beat together which results in an RF tone in the electrical domain (Green). A phase shift θ is applied to the optical carrier, and the resultant RF tone experiences a phase shift θ (Red). (b) Similarly, if the sideband in (a) is replaced with a broadband optical signal ($\delta\omega$), the resultant RF signal will have the same bandwidth as the optical signal (Green). A phase shift θ , is then applied to the optical carrier (Red) which results in the same broadband RF signal, but with a uniform phase shift θ .

The model predicts that the link deviations decreases with an increase in the phase enhancement factor with an ideal configuration. The analysis is relevant for both backward and forward Brillouin scattering, and hence, can also be applied to our previous work in a suspended silicon waveguide [25].

II. PRINCIPLE

The basic principle of a MWP phase shifter is shown in Fig. 1). The RF signal is transferred to the optical domain with an electro-optic modulator, a phase shift is then applied to the optical signal before it is detected at the photodetector. This process results in an RF signal in the electrical domain, however, the RF signal has a phase offset equal to the phase shift applied to the optical signal. The modulation process results in a carrier as well as an optical sideband, separated spectrally by the frequency of the input RF signal ω_{RF} as shown in Fig. 2(a)). The phase of the resultant RF signal is dependent on the difference in phase between the two optical tones, independent of how far the two tones are located from one another spectrally. So it is possible to control the phase of the output RF signal by controlling the phase applied to either the optical sideband or optical carrier. If

the optical phase shift is applied solely to the carrier, the output signal will experience a uniform phase shift, independent of the RF input frequency. Hence, this concept can be extended to broadband RF signals enabling high frequency, wide bandwidth signals to experience uniform phase shifts as shown in Fig. 2(b)).

In this paper, the phase shift is applied with Stimulated Brillouin scattering, which is a third-order nonlinear effect based on the interaction of the Stokes wave with frequency ω_s and a counter-propagating pump wave with frequency ω_p . The two optical waves are coupled through an acoustic wave with frequency Ω [27], generating a narrow-band moving index grating [21]. The pump wave coherently amplifies the Stokes wave which is accompanied by a dispersive narrowband phase shift at the Stokes frequency [21], [28]. This process needs to fulfill energy conservation given by $\Omega = \omega_p - \omega_s$ as well as momentum conservation given by $\vec{K}(\Omega) = \vec{K}(\omega_p) - \vec{K}(\omega_s)$ where $\vec{K}(\Omega)$ is the wavevector of the acoustic wave and $\vec{K}(\omega_{s/p})$ is the wavevector of the pump and Stokes waves, respectively. The Brillouin-induced phase shift is a result of the Kramers-Kronig relations [29]. Which states that a perturbation in the amplitude of a signal has a corresponding change in the refractive index [30]. The linewidth of the Brillouin response and corresponding phase shift is related to the inverse of the phonon lifetime, τ in the nonlinear medium [31]. To achieve a 360° phase shift, an impractical amount of Brillouin gain is required [23]. While a 360° phase shift is achievable in fiber, it only allows for a small carrier signal, otherwise, the Brillouin gain is saturated due to pump depletion at high signal powers [32]. Achieving a 360° phase shift is even more challenging in an optical chip, where record-high Brillouin gain in optimized chalcogenide waveguides achieving 52 dB of gain could only enable a $\pm 160^\circ$ phase shift [33].

Due to this limitation in Brillouin gain in integrated waveguides a technique to enhance the phase shift is required to achieve a microwave phase shifter that covers the full range of 360° . RF interference has been shown to enhance the performance of microwave filter as well as tunable delays [34]–[37]. It was recently shown that phase enhancement despite being interferometric in nature allows to enhance the phase for broadband signals by acting on the optical carrier [25]. The phase enhancement scheme only requires a small amount of Brillouin gain to achieve a large phase shift, so materials with other desirable properties, such as silicon, can be used even if they are not able to achieve high levels of Brillouin gain [25].

To implement this phase enhancement scheme, two spectrally separated optical signals are fed into a phase modulator, so their respective sidebands are out of phase from one another. The lower sideband from the lower frequency laser (Laser 2) is removed, while the upper sideband from the higher frequency laser (Laser 1) is removed. This leaves Carrier 2 (C_2) and Sideband 2 (SB_2) to beat at the photodetector to form $\vec{R}\vec{F}_\pi$, and Carrier 1 (C_1) and Sideband 1 (SB_1) to form $\vec{R}\vec{F}_0$ which is 180° out of phase to $\vec{R}\vec{F}_\pi$ (Fig. 3(a)). However, the amplitudes of C_2 and SB_2 are set to be larger than C_1 and SB_1 , so $\vec{R}\vec{F}_\pi$ has a larger amplitude than $\vec{R}\vec{F}_0$. The addition of $\vec{R}\vec{F}_0$ and $\vec{R}\vec{F}_\pi$ results in destructive interference, which forms a net vector $\vec{R}\vec{F}_{\text{net}}$ (Fig. 3(b)). The phase of $\vec{R}\vec{F}_\pi$ is then defined as the reference

phase for the phase enhanced scheme. $\vec{R}\vec{F}_\pi$ was chosen to be the reference phase as it represents the phase at which no Brillouin gain is applied. When Brillouin gain is applied to C_1 , this results in a phase shift θ_{SBS} as well as an increase in the length of the vector $\vec{R}\vec{F}_0$. This in turn, induces a phase shift of θ_{enh} of the resultant vector $\vec{R}\vec{F}_{\text{net}}$, which is enhanced due to vector addition (Fig. 3(c)).

The interference occurs in the electrical domain and the RF vectors are determined by the difference in phase between each sideband and the respective carrier. Note, the resultant RF tone does not depend on the phase between two lasers. However, ensuring a stable carrier frequency would help prevent the effects of dispersion through preventing the optical carrier from drifting into non-favorable regimes. In this instance, dispersion could result from the combined effects of the modulator, filter roll-offs and other components in the system. Ensuring the carrier does not spectrally drifts is important as dispersion could potentially change the phase relationship between the optical tones, which in turn would distort the phase of $\vec{R}\vec{F}_{\text{enh}}$.

A useful tool for visualizing the phase and amplitude information for RF phase shifters is the complex plane. The X-axis represents the real component while the Y-axis represents the imaginary component. The magnitude of the signal corresponds to the length of the vector spanning from the origin to the response, and the phase of the resultant signal is given by the angle of the vector. A complex plane diagram is depicted in Fig. 3(d)). Brillouin scattering is able to induce a gain-based phase shift, whereby sweeping through the Brillouin resonance, varied phase shifts can be applied while simultaneously varying the signal amplitude. The relationship between gain and phase can be represented in the complex plane and is depicted in red in Fig. 3(d)). However, when the destructive interference from $\vec{R}\vec{F}_\pi$ is applied, the response in the complex plane shifts in the direction of $\vec{R}\vec{F}_\pi$ to encompass the origin. After the interference from $\vec{R}\vec{F}_\pi$ the origin is totally enveloped by the response, which represents a 360° phase shift as shown in green in Fig. 3(d)). It is worth noting that to achieve a full 360° phase tuning range, the pump must sweep through the entire Brillouin resonance. In order to reduce amplitude fluctuations of $\vec{R}\vec{F}_{\text{net}}$, the length of the vector $\vec{R}\vec{F}_\pi$ is configured, such that it has a magnitude equal to the average magnitude of $\vec{R}\vec{F}_{\text{SBS}}$ over the entire Brillouin response to ensure that the resultant response is centered around the origin. Due to the interferometric nature of the phase enhancement scheme, there is an inherent trade-off between link gain and phase enhancement factor which we will investigate in the next section.

III. THEORETICAL ANALYSIS

In this section, we develop a theoretical model for the amplitude and phase response in the phase enhanced configuration. The Brillouin gain and phase response in a medium can be described with the following equations [21], [23].

$$M(\omega) = \exp\left(\frac{G}{2} \frac{\Gamma_B^2}{4\Delta\omega^2 + \Gamma_B^2}\right) \quad (1)$$

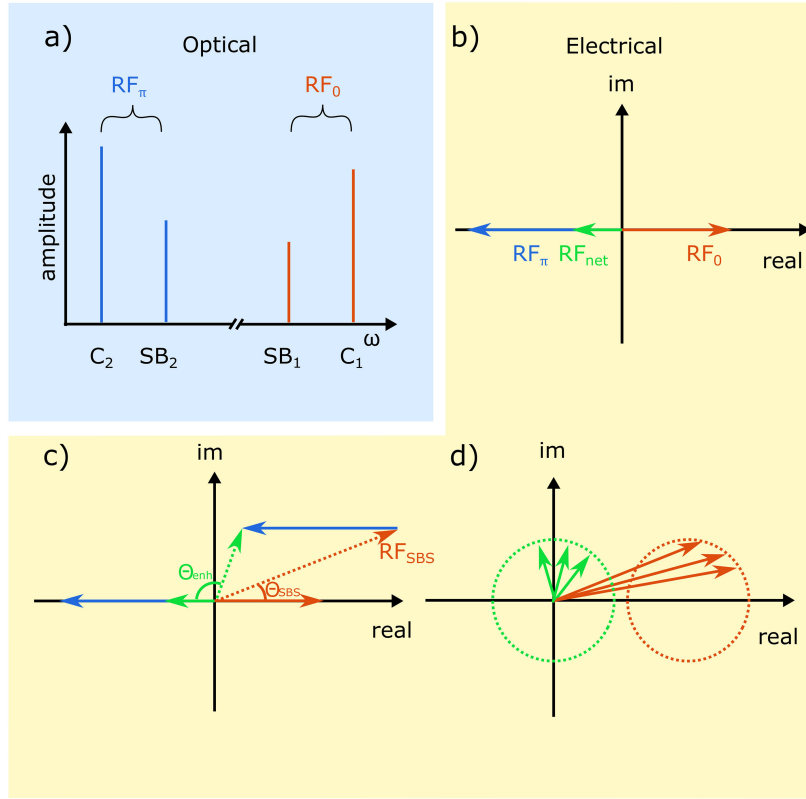


Fig. 3. (a) The phase enhancement scheme in the optical domain. Two pairs of carrier and sideband propagate together with each pair spectrally separated from one another. The phase between the lower sideband carrier pair (C_2, SB_2) is set to have a 180° difference to the upper carrier sideband pair (C_1, SB_1). Brillouin gain is then only applied to C_1 . (b) The carriers and sidebands beat to form \vec{RF}_0 and \vec{RF}_π respectively in the electrical domain. The amplitude and phase information is plotted on the complex plane. \vec{RF}_0 and \vec{RF}_π interfere to form the resultant vector \vec{RF}_{net} . (c) When Brillouin gain is applied to C_1 in the optical domain, the vector \vec{RF}_0 experiences a gain based phase shift and is relabeled as \vec{RF}_{SBS} . Through vector addition, the angle of the resultant vector \vec{RF}_{net} (θ_{enh}) is larger than the angle of \vec{RF}_{SBS} (θ_{SBS}). (d) As the pump is swept through the Brillouin resonance, the response of \vec{RF}_{SBS} traces a circle in the complex plane for small amounts of Brillouin gain. Through destructive interference, the resultant vector \vec{RF}_{net} also traces a circle in the complex plane, but it is centered around the origin which represents a 360° phase shift.

The Brillouin gain is given in terms of the power dependent variable G . Note: this equation is described in terms of the electric field, hence the factor of $\frac{1}{2}$. In Eq. 1, 2, Γ_B is the Brillouin linewidth, $\Delta\omega = \omega_p - \Omega_B - \omega$ is the offset frequency from the center of the Brillouin response. The phase response is given by [21], [23]:

$$\theta_{SBS}(\omega) = -G \Gamma_B \frac{\Delta\omega}{4\Delta\omega^2 + \Gamma_B^2} \quad (2)$$

The ideal Brillouin gain and phase response have been plotted in Fig. 4. We define the G parameter as:

$$G = \frac{g_0}{A_0} P_p(0) L_{eff} \quad (3)$$

Where g_0 is the gain coefficient of the medium, A_0 is the acousto-optic effective area, $P_p(0)$ is the pump power launched into the medium and L_{eff} is the effective length, calculated as:

$$L_{eff} = \frac{1}{\alpha} (1 - \exp(-\alpha L)) \quad (4)$$

Where α is the attenuation coefficient and L is the physical length of the medium.

We want to calculate the phase and amplitude enhancement factors. These parameters multiply with the phase and amplitude

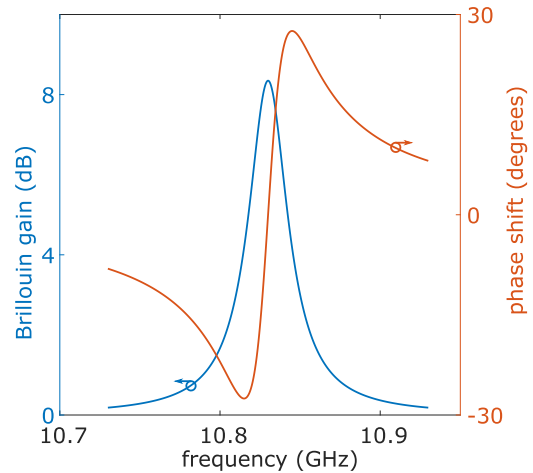


Fig. 4. Blue: Calculated Brillouin amplitude response for a 500 m long standard silica fiber using 20 mW of pump power. Orange: Corresponding phase response.

parameters of Brillouin vector, \vec{RF}_{SBS} , to form the combined phase shifter response. A 360° phase shift can be obtained from any amount of Brillouin gain through tailoring the destructive

interference from the phasor $\vec{R}\vec{F}_\pi$. It is possible to tailor the interference vector $\vec{R}\vec{F}_\pi$ such that the resultant phase is enhanced, but to less than 360° . However, for this analysis we will only be considering the case of a 360° phase shift. The phase enhancement factor, k_p is defined as:

$$k_p = \frac{2\pi}{\Delta\theta} \quad (5)$$

Where $\Delta\theta$ is the total range the phase can be tuned over from a given Brillouin response. The amplitude gain factor k_{Amp} is simply defined as the ratio of the phase enhanced output field amplitude divided by the un-enhanced output amplitude:

$$k_{Amp} = \frac{A_{enh}}{M(\omega)} \quad (6)$$

Where A_{enh} is the amplitude of the RF signal signal in the phase enhanced configuration and $M(\omega)$ is the amplitude of the un-enhanced output.

A. Phase Enhancement Factor

To calculate the phase enhancement factor, we need to find the maximum range the phase can be tuned over for a given Brillouin response. The frequency of the extrema can be found by differentiating Eq. 2 with respect to frequency. The maximum was found to be:

$$\Delta\omega = \pm \frac{\Gamma_B}{2} \quad (7)$$

The derivation can be found in Appendix A.

From this, we can calculate the total range the phase is tunable over.

$$\Delta\theta = \left| \theta_{SBS} \left(\frac{-\Gamma_B}{2} \right) \right| + \left| \theta_{SBS} \left(\frac{\Gamma_B}{2} \right) \right| = \frac{G}{2} \quad (8)$$

Therefore, substituting this into Eq. 5 we can calculate the phase enhancement factor to be:

$$k_p = \frac{4\pi}{G} \quad (9)$$

B. Amplitude Gain Factor

The RF interferometry procedure subtracts the phasor $\vec{R}\vec{F}_\pi$, from the initial SBS phasor, $\vec{R}\vec{F}_{SBS}$. $\vec{R}\vec{F}_\pi$ is set to have a magnitude equal to the average of the maximum and minimum magnitudes of $\vec{R}\vec{F}_{SBS}$ over the entire SBS resonance. This is to ensure that the center of the complex plane response after enhancement is located at the origin, enabling the vector $\vec{R}\vec{F}_{net}$ to rotate 180° between the points of no Brillouin gain and maximum Brillouin gain. In the un-depleted, low G regime, the SBS response approximately traces out a circle in the complex plane; this is shown in Fig. 5.

To calculate the amplitude of $\vec{R}\vec{F}_\pi$, we need to find the average amplitude of the maximum and minimum values of $\vec{R}\vec{F}_{SBS}$ throughout the entire Brillouin resonance to ensure the resultant response is centered around the origin as seen in Fig. 6. The maximum and minimum amplitudes of the SBS response can be found from Eq. 1. The maximum lies at $\Delta\omega = 0$ with a magnitude of $M(0) = \exp(\frac{G}{2})$ and the minimum lies far off-resonance where

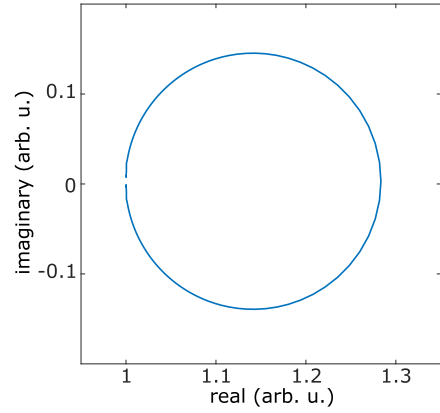


Fig. 5. Complex plane diagram of the Brillouin response in the un-enhanced configuration. The response is approximately circular for low values of G. Here G is equal to 0.5. This response comes from equations Eq. 1 and Eq. 2.

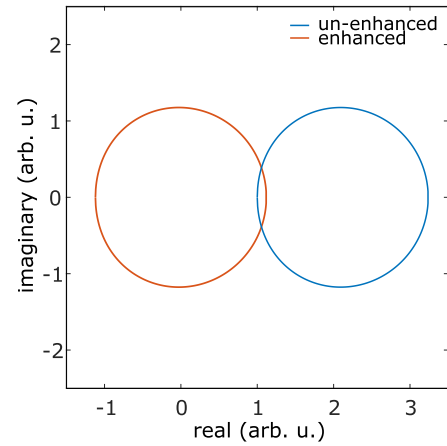


Fig. 6. Complex plane representation of the theoretical phase enhanced (orange) and un-enhanced (blue) configurations for a G of 2.35. The complex plane response shifts to encapsulate the origin, demonstrating a 360° phase shift.

$M = 1$. From the average of these, we can calculate the phasor $\vec{R}\vec{F}_\pi$:

$$\vec{R}\vec{F}_\pi = \frac{1 + \exp(\frac{G}{2})}{2} \exp(i\pi) \quad (10)$$

From here, the total phase enhanced output is the addition of the interference phasor $\vec{R}\vec{F}_\pi$ with the Brillouin vector $\vec{R}\vec{F}_{SBS}$:

$$\begin{aligned} \vec{R}\vec{F}_{net} &= A_{enh} \exp(i\theta_{enh}) \\ &= M(\omega) \exp(i\theta_{SBS}(\omega)) - \frac{1 + \exp(\frac{G}{2})}{2} \end{aligned} \quad (11)$$

Where A_{enh} and θ_{enh} are the amplitude and phase of the phase enhanced output, $M(\omega)$ and $\theta_{SBS}(\omega)$ are from Eq. 1 and Eq. 2 (θ_{SBS} from Fig. 3(c)) respectively.

The amplitude of A_{enh} can then be written as:

$$\begin{aligned} A_{enh} &= \sqrt{(M(\omega) \cos(\theta_{SBS}(\omega)) - |\vec{R}\vec{F}_\pi|)^2 + (M(\omega) \sin(\theta_{SBS}(\omega)))^2} \end{aligned} \quad (12)$$

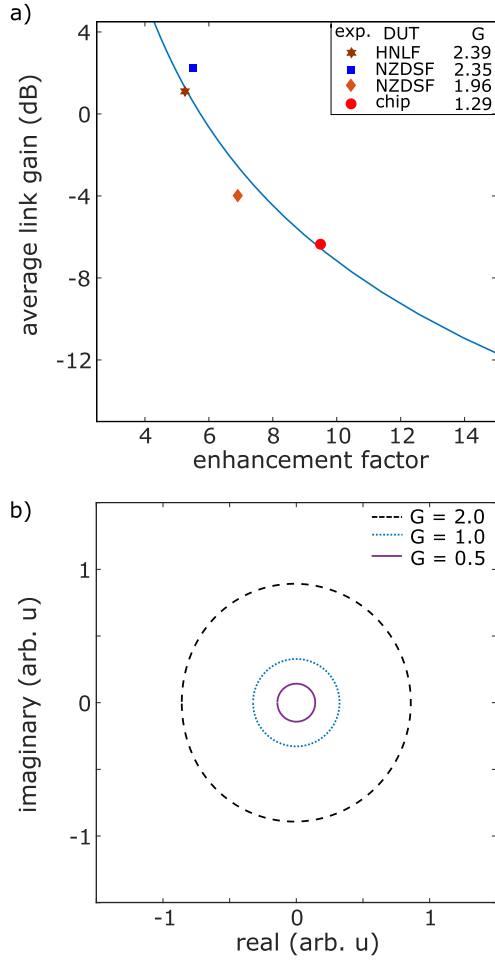


Fig. 7. (a) Depicts the link tradeoff under ideal conditions to achieve a 360° phase shift calculated from the model with the data points from the measurements superimposed. As the phase enhancement factor is increased, the average link gain decreases. (b) Theoretical complex plane response for three typical Brillouin gain values. At higher levels of link gain, the circular plot has a larger radius. Black (dashed line), $k_p = 6.2$ and $G = 2$; Blue (dotted line), $k_p = 12$ and $G = 1$; Purple (solid line), $k_p = 25$ and $G = 0.5$.

From Eq. 6, the amplitude gain factor is A_{enh} divided by the amplitude of the un-enhanced Brillouin output, $M(\omega)$, leading to:

$$k_{\text{Amp}} = \frac{\sqrt{(M(\omega)\cos(\theta_{\text{SBS}}(\omega)) - |\vec{R}\vec{F}_\pi|^2 + (M(\omega)\sin(\theta_{\text{SBS}}(\omega)))^2}}{M(\omega)} \quad (13)$$

Here, we are interested in the resultant link gain which is given by the term A_{enh} . The RF link gain was plotted against the phase enhancement factor in Fig. 7(a). The ideal link gain in Fig. 7(a,b) is determined by calculating the average magnitude over the 360° tuning range, and is measured relative to an ideal link with a link gain of 0 dB. Data points from the experimental measurements in different optical fibers as well as the photonic chip are added to Fig. 7(a) and confirm the trend given by the theoretical model. A larger phase enhancement corresponds

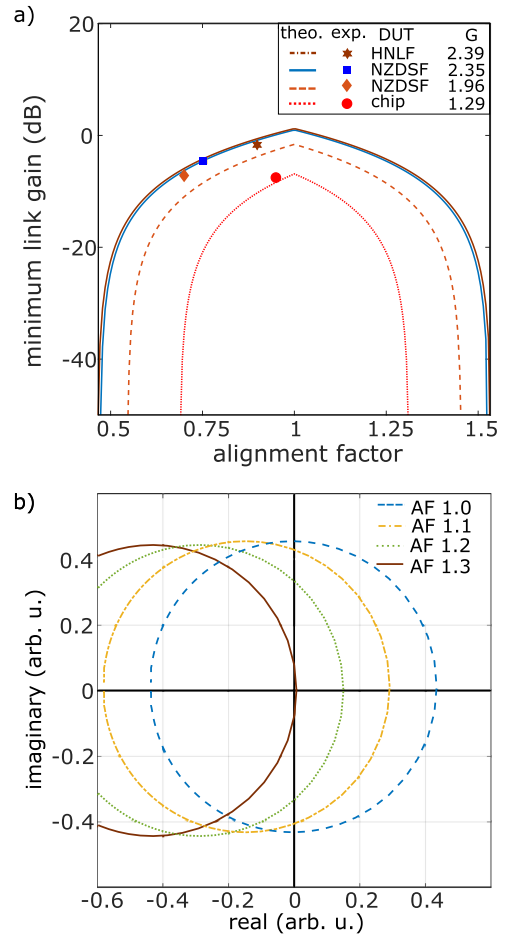


Fig. 8. (a) Calculated curves from the model as well as experimental data points of the minimum link gain for different alignment factors (AF) of the interfering RF vectors. Brown (dashed dotted line), phase enhancement factor of 5.25 ($G = 2.39$); Blue (solid line), phase enhancement factor of 5.35 ($G = 2.35$); Orange (dashed line), phase enhancement factor of 6.4 ($G = 1.96$); Red (dotted line), phase enhancement of 9.7 ($G = 1.29$). (b) The complex plane representation is depicted for a phase enhancement factor of 10. As $\vec{R}\vec{F}_\pi$ becomes more misaligned, the circular response moves off-center, so the minimum point is closer to the origin. Blue (dashed line), AF = 1; Orange (dashed-dotted line), AF = 1.1; Green (dotted line), AF = 1.2; Brown (solid line), AF = 1.3.

to a larger reduction in the link gain due to a higher degree of destructive interference from $\vec{R}\vec{F}_\pi$. This manifests in the complex plane as a smaller circular response around the origin as shown in Fig. 7(b).

However, this assumes that the amplitude of vector $\vec{R}\vec{F}_\pi$ is set correctly as calculated in Eq. 10. If the magnitude or angle of the interference vector deviates from the ideal case, there will be a reduction in performance. In this section, we will analyze the effect of variation in the magnitude of $\vec{R}\vec{F}_\pi$, the effect of varying the angular offset can be seen in Appendix C. If the length of $\vec{R}\vec{F}_\pi$ deviates from the ideal case, there will be a reduction in the minimum RF link gain and an increase in the link deviation as shown in Fig. 8 and Fig. 9. The alignment factor (AF) is defined as the amplitude of $\vec{R}\vec{F}_\pi$ divided by the average amplitude of $\vec{R}\vec{F}_{\text{SBS}}$ over the Brillouin resonance. When the alignment factor is set to 1 the resultant phase enhanced response is centered around the origin of the complex plane.

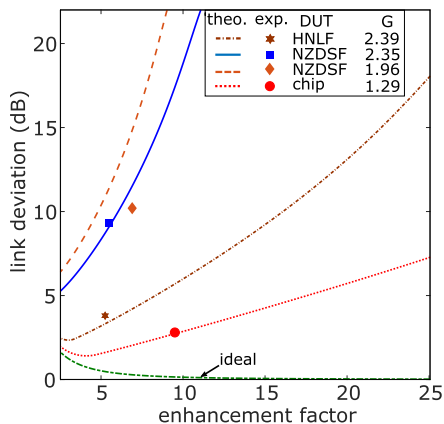


Fig. 9. Model of the link deviation with enhancement factor. For perfect alignment the link deviation is greatly reduced (green dashed curve). However, any misalignment concerning the RF vectors greatly increases the link deviation. Orange (dashed line) AF = 0.7; Blue (solid line), AF = 0.75; Brown (dashed dotted line) AF = 0.9; Red (dotted line), AF = 0.95; Green, ideal response, AF = 1.

In the case of a large phase enhancement factor, there will only be a relatively small amount of Brillouin gain applied to $\vec{R}\vec{F}_0$. This will result in the complex plane response tracing out a circle with a small radius, which will be sensitive to misalignment when compared to a system with a smaller enhancement factor, which will have a larger radius in the complex plane. This can be seen in Fig. 8(a) which plots the minimum link gain throughout the Brillouin resonance against the alignment factor. The RF link gain for a system with a phase enhancement factor of 6.4 (orange) decays less rapidly than the system with a phase enhancement factor of 25 (Purple) when the magnitude of $\vec{R}\vec{F}_\pi$ is increased.

As the length of $\vec{R}\vec{F}_\pi$ changes, the location of the resultant response traced by $\vec{R}\vec{F}_{net}$ is also affected on the complex plane. This affects the amplitude response of the phase enhanced output. Additionally, if the response traced by $\vec{R}\vec{F}_\pi$ intersects the origin, there will be complete destructive interference and a loss of signal at that point. This can be seen in Fig. 8(a) with the steep decline of RF link gain and the corresponding complex plane response in Fig. 8(b)). The alignment factors for the measurements presented in Section IV are shown in Fig. 8(a)). If the response in the complex plane is shifted too far by $\vec{R}\vec{F}_\pi$, the complex response will no longer encapsulate the origin so a 360° phase shift will no longer be possible. Additionally, the amount of link deviation throughout the Brillouin resonance also increases as the magnitude of $\vec{R}\vec{F}_\pi$ deviates further from the ideal value. This can be visualized by the complex plot in Fig. 8(b)), as the magnitude of the vector $\vec{R}\vec{F}_{net}$ varies more throughout the Brillouin resonance the further offset the response is from the origin.

The model predicts in the ideal case that a larger phase enhancement factor would result in a reduced link deviation, as can be seen in green in Fig. 9. However Fig. 9 also shows that if the interfering vectors are misaligned the link deviation can increase for larger phase enhancement factors. The link deviations of the measurements presented in Section IV are displayed in the figure.

To summarize the key findings of the analysis, for an increased phase enhancement factor there will be a reduction in the required Brillouin gain and hence the power required to achieve a 360° phase shift. Assuming the interferometric components have been set correctly, the model predicts the possibility of very small deviations in the link gain over the 360° phase shift. On the other hand, the model also predicts an increased sensitivity to the alignment of the interfering vector components as the phase enhancement factor k_p increases. If the vectors are not correctly balanced, the link deviation increases with larger enhancement factors. This explains the deviations of the link gain in the experimental data presented in the following section.

IV. EXPERIMENT

The experimental setup of our SBS phase shifter is shown in Fig. 10. The optical signal from a narrow linewidth distributed feedback (DFB) laser (laser 1) is split into two paths, the pump path, and the signal path. The optical carrier in the pump path is up-converted with a dual parallel Mach Zehnder modulator (DPMZM) biased for single-sideband suppressed carrier modulation and amplified afterward with an erbium-doped fiber amplifier (EDFA) before propagating through the Brillouin gain medium, referred to as device under test (DUT). The RF input is modulated upon the optical carrier in the signal path using a phase modulator, before continuing to the DUT. The DUT used in this case is either a length of optical fiber, or an integrated chalcogenide waveguide. The optical chip has an integrated chalcogenide rib waveguide structure with dimensions of $0.850 \mu\text{m} \times 2 \mu\text{m}$ with an etch depth of 35% and 12 cm in length. The total waveguide insertion loss is 15.5 dB consisting of 4 dB coupling loss per facet using edge coupling with lensed fibers.

The pump induces an SBS phase shift on the carrier through the SBS process, before being filtered and continuing to the photodetector to generate the RF output. To achieve the phase-enhanced output, a second optical carrier (laser 2) is inserted (dotted green box), which co-propagates through the phase modulator and DUT but does not experience a Brillouin interaction. The wavelength of lasers 1 and 2 was set around the zero dispersion point in the fiber to reduce distortion. Each optical carrier has opposing sidebands removed to ensure the resultant RF tones are 180° out of phase after beating at the photodetector. The phase of $\vec{R}\vec{F}_\pi$ was measured on the vector network analyzer to ensure it was 180° out of phase relative to $\vec{R}\vec{F}_0$ before the pump was turned on. Any small adjustments in the phase of $\vec{R}\vec{F}_\pi$ or $\vec{R}\vec{F}_0$ could be controlled for by tuning the polarization before the modulator.

A. Fiber-Based MWP Phase Shifter

Initially, the SBS gain and phase response was measured in a 30 m length of highly-nonlinear-fiber (HNLf) as seen in Fig. 11 (blue dashed curve), the corresponding theoretical value can be seen in the solid yellow line. The measurement was achieved by sweeping an optical probe signal through the Brillouin resonance using a vector network analyzer (VNA). The Brillouin shift was measured to be around 9.4 GHz. The phase response measured

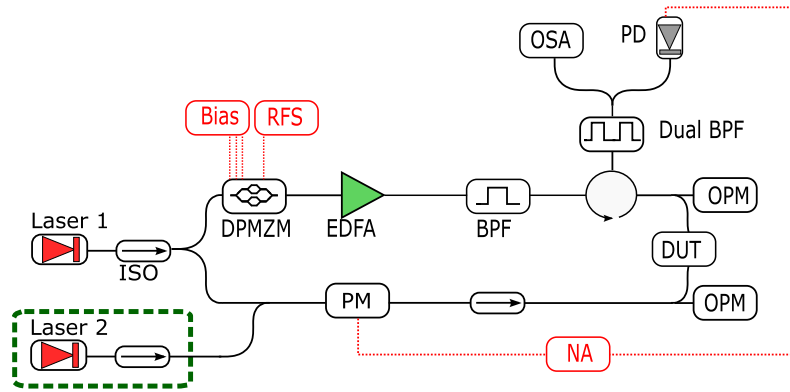


Fig. 10. Experimental setup. The phase enhancement laser is shown in the dotted green box. DUT: device under test; NA: Network analyzer; OPM: optical power meter; PM: phase modulator; ISO: isolator; EDFA: erbium doped fiber amplifier; DPMZM: dual parallel Mach Zehnder modulator; PD: photodetector; OSA: optical spectrum analyzer; BPF: band pass filter; RFS: radio frequency source.

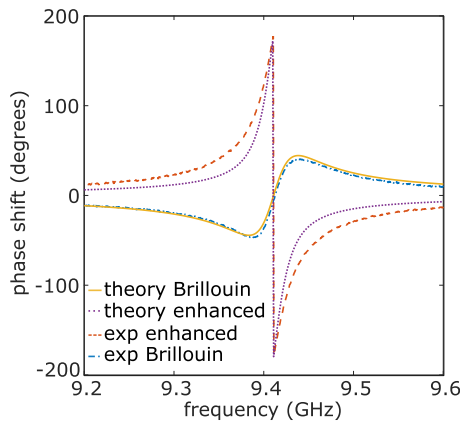


Fig. 11. Theoretical and experimental Brillouin phase response in highly non-linear optical fiber. There is a minor phase offset in the un-enhanced Brillouin response due to experimental uncertainty, this offset was then amplified by the phase enhanced scheme, leading to the small discrepancy between the theory and measurement of the enhanced phase responses in the figure. Blue (dashed-dotted line), experimental measurement with no phase enhancement; Orange (dashed line), experimental measurement with phase enhancement; Yellow (solid line), theoretical result with no phase enhancement; Purple (dotted line), theoretical result with phase enhancement.

here was found to be $\pm 40^\circ$ which corresponds to a Brillouin gain of 12.5 dB. The additional out-of-phase RF signal was then connected to operate in the phase enhanced regime, and using the same amount of pump power a $\pm 180^\circ$ phase response was seen in Fig. 11 (red dashed line) with the corresponding theoretical result shown with the purple dotted line. This corresponds to a phase enhancement factor of 4.5. The deviation between the theory and the experiment could potentially be explained due to the drift in the bias of the modulator, polarization, laser wavelength, EDFA power. This offset was then enhanced with the phase enhanced scheme, resulting in a larger mismatch for the enhanced response.

The experiment was then adjusted to the broadband configuration. The frequency of the optical pump was tuned by the DPMZM to act on the optical carrier instead of the sidebands. This enables the sideband to sweep over a broad range, limited only by the bandwidth of the modulator and photodetector

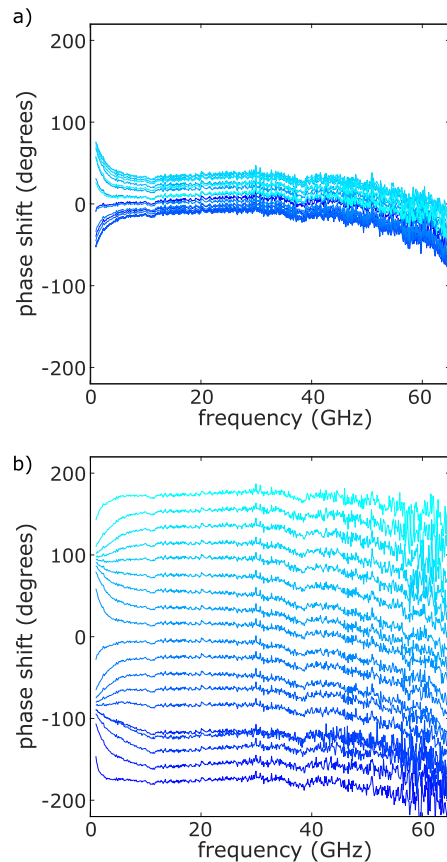


Fig. 12. (a) Ultra-broadband phase shift in fiber without phase enhancement. (b) Ultra-broadband 360° phase shift in fiber with a phase enhancement factor, $k_p = 6.4$.

while experiencing a uniform phase shift. The RF input to the phase modulator was swept from 0.1 GHz to 65 GHz as seen in Fig. 12(a)). This shows a broadband $\pm 25^\circ$ phase shift from 7.6 dB of Brillouin gain in the 40 m length of non-zero dispersion-shifted-fiber (NZDSF). The phase can be adjusted through varying the Brillouin resonance by adjusting the RF drive frequency to the DPMZM. The phase enhancement laser was then connected and using the same optical pump power a

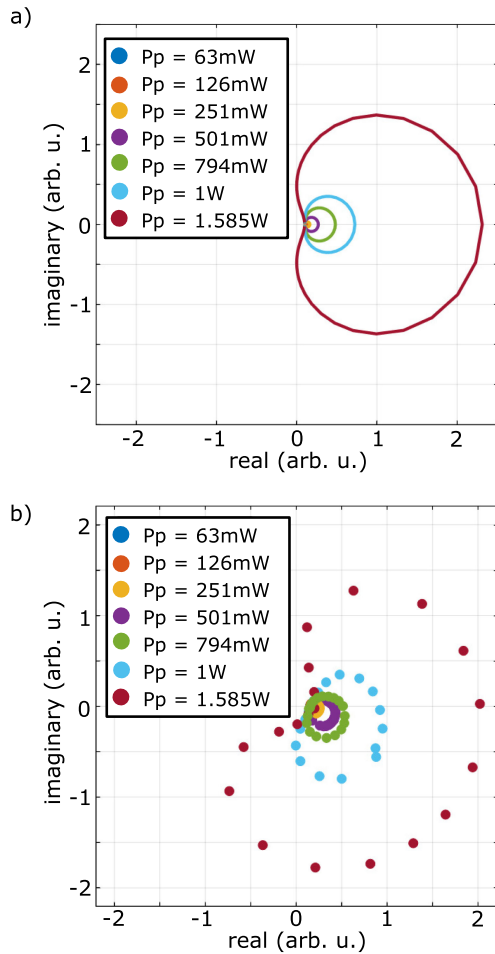


Fig. 13. Complex plane diagram of the un-enhanced phase and amplitude response in non-zero dispersion-shifted fiber. (a) The theoretical complex plane response. The shape is almost a circle for low values of G but becomes distorted at higher levels of Brillouin gain. (b) Experimental results conducted in non-zero dispersion-shifted-fiber. The results are similar in shape but have been rotated at large values of G .

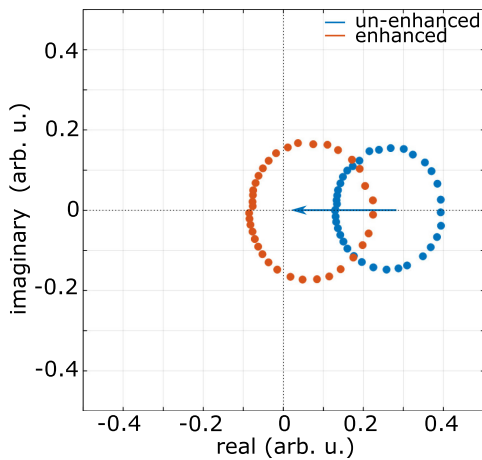


Fig. 14. Complex representation of the broadband phase shift in fiber. The un-enhanced values are located to the side of the origin, with the maximum achievable phase shift given by the angle relative to the origin, and the link variation a function of the distance to the origin (blue). When the interference component $\Re\{F_\pi\}$ is added, the complex plane response moves to encapsulate the origin, demonstrating a 360° phase shift. The enhancement factor k_p is 5.35 with a corresponding G value of 2.35.

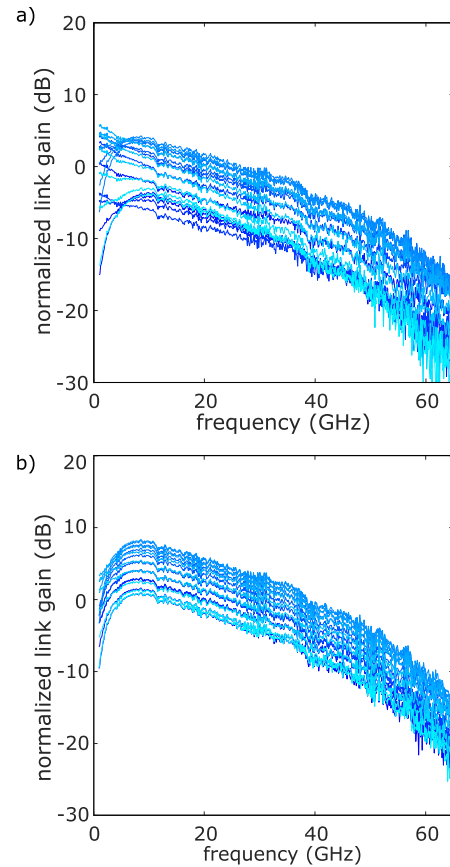


Fig. 15. (a) Normalized broadband RF gain in non-zero-dispersion-shifted-fiber without phase enhancement (b) and with phase enhancement factor of 6.4.

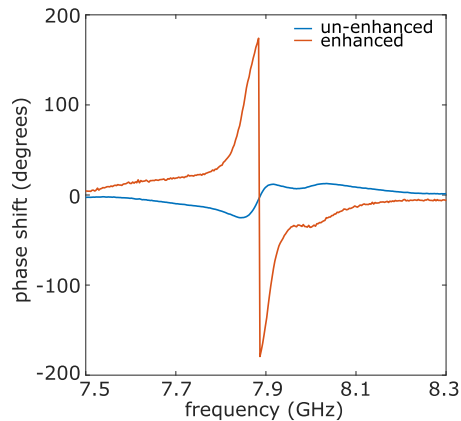


Fig. 16. Brillouin phase profile in an integrated chalcogenide waveguide with no phase enhancement (blue) and with phase enhancement (orange).

360° phase shift was obtained, representing a phase enhancement factor of 6.4 as shown in Fig. 12(b)).

The un-enhanced response was then plotted in the complex plane (Fig. 13). Fig. 13(b)) shows the average value of the amplitude and phase response over the frequency range from 20 GHz to 33 GHz for each of the un-enhanced phase and amplitude measurements plotted in the complex plane. Fig. 13(a)) depicts the theoretical response calculated from equations (1) and (2). For small values of G , the response is approximately circular,

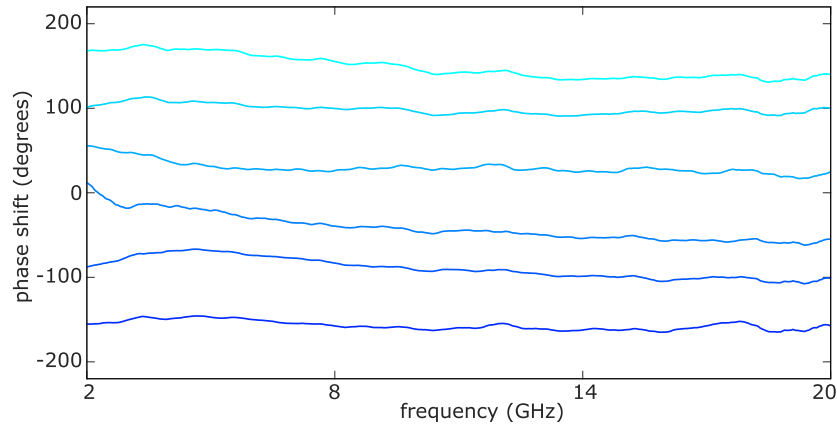


Fig. 17. Broadband phase shift in an integrated chalcogenide waveguide. The phase enhancement factor here is 9.5.

but as G increases, the distortion in the circular shape increases. The experimental results measured in fiber plotted in Fig. 13(b) depict similar results, showing the transition from the circular case into the distorted form. However, the response has been rotated, which we suspect is due to mismatched polarization states between the optical pump and C_1 or potentially due to drift in the bias of the modulator, laser wavelength or EDFA power throughout the duration of the experiment.

The complex plane diagram for a broadband phase shifter with a G of 2.35 is depicted in Fig. 14. The un-enhanced response is approximately centered on the X axis, due to the relatively low value of G used for that measurement, which is consistent with Fig. 13(b) where a significant rotation and distortion in the circular shape is only seen with large values of G . Similar to the un-enhanced phase response, the link gain and phase were averaged over 20 GHz to 33 GHz and were plotted on a complex plane. The un-enhanced response (blue curve) is centered at a significant offset to the right of the origin. The response will need to grow considerably to encompass the origin, highlighting the large Brillouin gain required for a 360° phase shift. However, when the phase enhancement laser is applied, the midpoint of the complex plane response moves to encapsulate the origin (red curve). Note, here, the response is positioned off center. From Fig. 8, this would suffer from a larger link deviation over the Brillouin resonance when compared to the ideal case in Fig. 6.

The link gain in the broadband experiment is reduced at higher frequencies due to the response from the modulator and photodetector as seen in Fig. 15 which shows the link deviation with different phase shifts. When the phase shifter was operating in the phase enhanced configuration, there was an enhancement from $\pm 25^\circ$ to $\pm 180^\circ$ which incurred a reduction in link gain of 4 dB from an average value of -58 dB to -62 dB. This is larger than the loss predicted from Eq. 12 and can be attributed to a minor reduction in Brillouin gain due to a drift in polarization throughout the experiment. Additionally, the link deviation increased due to a misalignment of the vector RF_π .

B. Chip-Based MWP Phase Shifter

To demonstrate the concept of the chip-based phase shifter, the fiber was replaced with an integrated chalcogenide waveguide.

As with the fiber, initially, the gain and phase response of the integrated waveguide was measured as seen in Fig. 16. The Brillouin frequency in the waveguide was found to be 7.9 GHz, notably less than in fiber. The blue curve in Fig. 16 corresponds to an un-enhanced phase response of $\pm 19^\circ$. There is a minor asymmetry in the curve, which is due to a non-symmetric gain profile of the waveguide. Brillouin scattering is sensitive to the geometry of the waveguide, and the asymmetry could be due to variations in waveguide height [38], width [39] or interactions between multiple acoustic or optical modes [40]. Using the phase enhancement technique, we can enhance this to achieve a $\pm 180^\circ$ phase response, which is shown in orange in Fig 16.

The pump was adjusted to act on the carrier to demonstrate broad bandwidth operation using the same amount of pump power, in the same waveguide. In the phase enhanced configuration, a phase shift of $\pm 180^\circ$ was achieved, representing an enhancement factor of 9.5, approximately an order of magnitude, this is shown here in Fig. 17. This was achieved using 6 dB of Brillouin gain which was induced from a constant optical pump power of 19 dBm in the waveguide and sweeping through the Brillouin resonance. Smoothing has been applied to the raw data to remove interference likely induced by the pump back-reflection from the facets of the chip. A bandwidth of 18 GHz was achieved, which was limited by the bandwidth of available RF and optoelectronic components.

V. DISCUSSION AND CONCLUSION

In this work, we have demonstrated an ultra-broadband phase shifter using backward stimulated Brillouin scattering spanning a bandwidth of 65 GHz in optical fiber. We have also demonstrated a broadband phase enhancement factor of approximately an order of magnitude in an integrated chalcogenide waveguide. Additionally, we have developed a theoretical model for the phase enhancement scheme which predicts the favorable link gain reduction trade-off with phase enhancement and shows a reduction in link variation with an increase in phase enhancement factor compared to the un-enhanced case. Additionally, we have presented an in-depth analysis of how various parameters effect the operation of the phase shifter at different levels of phase enhancement. In particular, we have shown that at high levels of

phase enhancement k_p , there is a reduction in the average link as well as increased sensitivity to the alignment and magnitude of the interference phasor, RF_π . The misalignment of RF_π has the effect of increasing the link deviation and if the misalignment results in the enhanced response no longer encapsulating the origin, a 360° phase shift would no longer be possible. However, large values of k_p require only minimal amounts of Brillouin gain to achieve 360° phase shifts. Conversely, low values of k_p are less sensitive to misalignment of the interference component but requires more Brillouin gain. However, interestingly, the model predicts that for k_p less than 5.7 the destructive interference can be outweighed by the Brillouin gain component leading to a net increase in link gain. The work presented in this paper will enable large Brillouin-induced phase shifts from a low power, counter-propagating pump in an integrated form factor, which provides increased stability. This will in turn reduce the filtering requirements when compared to the forward Brillouin case. Additionally, due to the increased sensitivity from the interferometry, this scheme could also have applications in sensing and signal processing.

APPENDIX A

To calculate the phase enhancement factor, we need to find the maximum range the phase can be tuned over for a given Brillouin response. This can be found by differentiating the Brillouin phase response given in Eq. 2 with respect to frequency, to find where the maximums occur.

$$\theta_{\text{SBS}}(\omega) = -G\Gamma_B \frac{\Delta\omega}{4\Delta\omega^2 + \Gamma_B^2} \quad (14)$$

To find the maxima with respect to $\Delta\omega$:

$$\frac{d\theta_{\text{SBS}}(\Delta\omega)}{d\Delta\omega} = 0 \quad (15)$$

From the Quotient rule

$$\frac{8\Delta\omega(G\Gamma_B\Delta\omega) - (4\Delta\omega^2 + \Gamma_B^2)(G\Gamma_B)}{(G\Gamma_B\Delta\omega)^2} = 0 \quad (16)$$

$$\Rightarrow 4\Delta\omega^2 G\Gamma_B + \Gamma_B^3 G = 0 \quad (17)$$

$$\Rightarrow 4\Delta\omega^2 = \Gamma_B^2 \quad (18)$$

$$\Rightarrow \Delta\omega = \frac{\Gamma_B}{2} \quad (19)$$

To calculate the amplitude of A_{enh} , we need to find the length of the vector from the origin to the response in the complex plane. On the complex plane, the real component is plotted along the X-axis, while the imaginary component is plotted along the Y-axis. The real axis consists of the vector \vec{RF}_π , subtracted from the cosine of the Brillouin vector, which has a magnitude of $M(\omega)$ from Eq. 1 and a phase of $\theta_{\text{SBS}}(\omega)$ from Eq. 2.

$$\text{Real} = M(\omega)\cos(\theta_{\text{SBS}}(\omega)) - |\vec{RF}_\pi| \quad (20)$$

While the imaginary component consists only of the sine of the Brillouin vector.

$$\text{Imaginary} = M(\omega)\sin(\theta_{\text{SBS}}(\omega)) \quad (21)$$

Pythagoras' theorem is then used to calculate the length of the resulting amplitude A_{enh} .

$$A_{\text{enh}} = \left(\left(M(\omega)\cos(\theta_{\text{SBS}}(\omega)) - |\vec{RF}_\pi| \right)^2 + \left(M(\omega)\sin(\theta_{\text{SBS}}(\omega)) \right)^2 \right)^{\frac{1}{2}} \quad (22)$$

APPENDIX B

For applications in materials such as in SiN or planar silicon structures, Brillouin scattering may not be available. However, the phase enhancement technique can still be applied to enhance an initial phase shift. An alternate method is proposed here which would enable a large phase enhancement by tuning the amplitude of RF_π , something readily achievable.

In order to achieve the direct phase enhancement without Brillouin scattering, an initial vector with a phase shift θ_+ is required (\vec{RF}_{θ_+}). This vector is shown here in the complex plane in Fig. 18(a) (blue), which has a magnitude of one and an angle of 12° , however, the vector could have any nonzero magnitude and angle. A second optical signal generates the RF component \vec{RF}_π with a phase of π . \vec{RF}_π destructively interferes with \vec{RF}_{θ_+} to generate the resultant \vec{RF}_{net} . When the amplitude of \vec{RF}_π is increased, the vector \vec{RF}_{net} is rotated, leading to a large phase shift. The response traced by increasing the amplitude of \vec{RF}_π resembles a flat line in the complex plane as shown in Fig. 18(a). The angular phase offset θ_+ is required to be non-zero in order to generate a broad range of possible phase shifts as otherwise the resultant \vec{RF}_{net} would pass through the origin and only two phase states would be possible. With the configuration shown in Fig. 18(a) a phase tuning range of approximately 180° can be achieved, as seen in Fig. 18(b)). In order to reach the negative phase states, the initial phase shift θ_- would have to be a negative value (red curve in Fig. 18(a), (b))).

As the vector \vec{RF}_{net} rotates, the phase shift varies as does the link gain, shown in Fig. 18(c)). The RF link gain reaches a minimum at 90° where the vector is vertical, representing the closest point of the response to the origin of the complex plane. The link variation and minimum value of the link gain is dependent on the angle of the vector \vec{RF}_{θ_+} . This can be understood as: At larger values of θ_+ the further away the minimum value of the complex plane response would be from the origin. However, the phase tuning range would also be reduced, as phase values smaller than θ_+ would be inaccessible, unless the the phase of RF_{pi} is flipped 180° . Additionally, the plot in Fig. 18(c)) is symmetrical about 90° and there exists a point where the link of the resultant vector \vec{RF}_{net} is equal to the link gain of the original vector \vec{RF}_θ . It is also worth noting that a phase shift of 180° would not be obtainable as the length of \vec{RF}_π would asymptotically grow to reach that point. The phase of the resultant signal can be calculated with the following equation:

$$\theta_{\text{enh}} = \arctan \left(\frac{|\vec{RF}_\theta| \sin(\theta)}{|\vec{RF}_\theta| \cos(\theta) - |RF_\pi|} \right) \quad (23)$$

This scheme provides a convenient means to generate large phase shifts, however, the added complexity of the Brillouin approach comes with the advantage of reduced link variation.

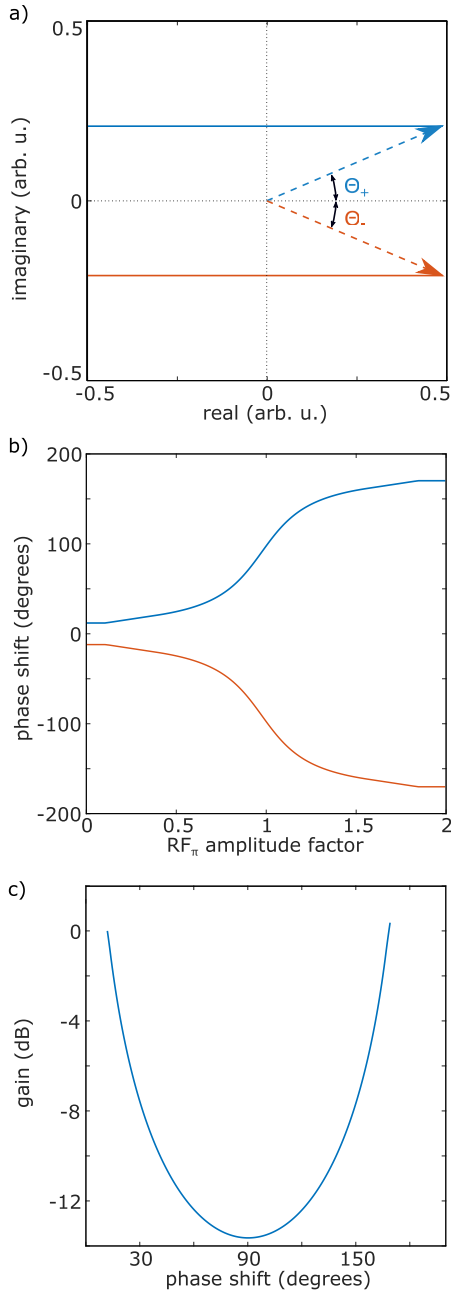


Fig. 18. It is possible to control the phase by varying the amplitude of $\vec{R}_{F_{\pi}}$. Here, the theoretical parameters of a phase enhancement factor of 15 are plotted. (a) The complex plane response; Blue, $\vec{R}_{F_{\theta_+}}$ has a magnitude of 1 and a phase of 12° ; Orange, $\vec{R}_{F_{\theta_-}}$ has a magnitude of 1 and a phase of -12° . (b) Phase response of the traces shown in (a). (c) As the phase is tuned over the range, the penalty to link gain varies with minimum transmission at 90° .

This is due to the circular Brillouin response in the complex plane at low levels of gain which inherently provides low link deviations if configured correctly.

APPENDIX C

So far, we have looked at the effect of varying the amplitude of $\vec{R}_{F_{\pi}}$. However, if the interference component is not π radians out of phase, there will also be a degradation in performance. Here, we analyze the effect of varying the angle of the interference component $\vec{R}_{F_{\text{int}}}$. If the angle of $\vec{R}_{F_{\text{int}}}$ has a non-zero angular

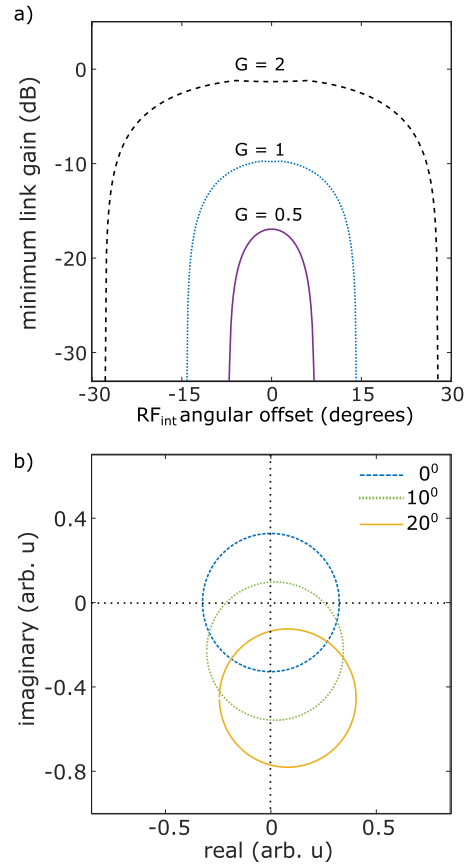


Fig. 19. (a) The link response is dependent on the angle of the vector $\vec{R}_{F_{\text{int}}}$, and the performance of the system degrades as the angle diverges from a 0° offset. The minimum value of the link gain throughout the Brillouin resonance is plotted against offset angle of $\vec{R}_{F_{\text{int}}}$ where the magnitude of $\vec{R}_{F_{\text{int}}}$ is set to the optimal value as defined in Eq. 10. Black (dashed line): phase enhancement factor, $k_p = 6.2$ ($G = 2$); Blue (dotted line): phase enhancement factor of $k_p = 12$ ($G = 1$); Purple (solid line): phase enhancement factor, $k_p = 25$ ($G = 0.5$). (b) Complex plane response for a phase enhancement factor of 12. Blue (dashed line): offset angle = 0° ; Green (dotted line): offset angle = 10° ; Yellow (solid line): offset angle = 20° . Yellow does not encapsulate the origin, so a 360° phase shift is not possible.

offset from the ideal value, the response traced by $\vec{R}_{F_{\text{net}}}$ will no longer be centered around the origin of the complex plane. This is quite similar to the effect caused by misalignment in the magnitude of $\vec{R}_{F_{\pi}}$, as seen in Fig. 8(a) in that the points which comprise the resultant response are no longer equidistant from the origin. This in turn leads to a variation in the link gain along the response. In Fig. 19(a) the angle of $\vec{R}_{F_{\text{int}}}$ is plotted against the minimum value of link gain throughout the Brillouin resonance. If the angle of $\vec{R}_{F_{\text{int}}}$ is such that the response traced by $\vec{R}_{F_{\text{net}}}$ passes near to the origin, there will be a corresponding decline in the value of the minimum link gain, accounting for the steep decline in figure Fig. 19(a)). It is worth noting that there is a dip in the curves in Fig. 19(a), these are due to the non-circular complex plane response of Brillouin gain and become less significant with reduced levels of G as seen in Fig. 13). The calculated complex plane response for different angular offsets can be seen in Fig. 13(b)). Here, $k_p = 12$, and $G = 1$, with an angular offset of 0° in blue, 10° in green and 20° in yellow. For an angular offset of 20° , the response no longer encompasses the complex plane, so a 360° phase shift is no longer achieved.

REFERENCES

- [1] D. Marpaung, J. Yao, and J. Capmany, "Integrated microwave photonics," *Nature Photon.*, vol. 13, pp. 80–90, Jan. 2019.
- [2] J. Capmany, B. Ortega, and D. Pastor, "A tutorial on microwave photonic filters," *J. Lightw. Technol.*, vol. 24, no. 1, pp. 201–229, Jan. 2006.
- [3] R. C. Hansen, *Phased Array Antennas*. Hoboken, NJ, USA: Wiley, Jan. 1998.
- [4] A. Naqvi and S. Lim, "Review of recent phased arrays for millimeter-wave wireless communication," *Sensors*, vol. 18, Sep. 2018, Art. no. 3194.
- [5] Q. Cheng, A. Alomainy, and Y. Hao, "Near-field millimeter-wave phased array imaging with compressive sensing," *IEEE Access*, vol. 5, pp. 18975–18986, Oct. 2017.
- [6] W. Liu and J. Yao, "Ultra-wideband microwave photonic phase shifter with a 360° tunable phase shift based on an erbium-ytterbium co-doped linearly chirped FBG," *Opt. Lett.*, vol. 39, pp. 922–924, Feb. 2014.
- [7] M. Attygalle and D. Stepanov, "Phase manipulation of RF signals using a fiber Bragg grating with step group delay profile," in *Proc. Adv. Photon. Congr.*, 2012, Paper BW2E.5.
- [8] S. T. Winnall, A. C. Lindsay, and G. A. Knight, "A wide-band microwave photonic phase and frequency shifter," *IEEE Trans. Microw. Theory Techn.*, vol. 45, no. 6, pp. 1003–1006, Jun. 1997.
- [9] E. H. W. Chan, W. Zhang, and R. A. Minasian, "Photonic RF phase shifter based on optical carrier and RF modulation sidebands amplitude and phase control," *J. Lightw. Technol.*, vol. 30, no. 23, pp. 3672–3678, Dec. 2012.
- [10] Z. Guo and J. Ma, "Microwave photonic phase shifter with a full 360° tunable range based on polarization sensitive electro-optical phase modulator and polarization modulator," *Opt. Eng.*, vol. 57, Aug. 2018, Art. no. 086109.
- [11] E. Chan, "Microwave photonic phase shifter based on a nonreciprocal optical phase shifter inside a Sagnac interferometer," *Opt. Commun.*, vol. 324, pp. 127–133, Aug. 2014.
- [12] A. Loayssa and F. J. Lahoz, "Broad-band RF photonic phase shifter based on stimulated Brillouin scattering and single-sideband modulation," *IEEE Photon. Technol. Lett.*, vol. 18, no. 1, pp. 208–210, Jan. 2006.
- [13] P. Minzioni *et al.*, "Roadmap on all-optical processing," *J. Opt.*, vol. 21, May 2019, Art. no. 63001.
- [14] M. Burla, L. R. Cortes, M. Li, X. Wang, L. Chrostowski, and J. Azana, "On-chip ultra-wideband microwave photonic phase shifter and true time delay line based on a single phase-shifted waveguide bragg grating," in *Proc. IEEE Int. Topical Meeting Microw. Photon.*, Oct. 2013, pp. 92–95.
- [15] Q. Chang, Q. Li, Z. Zhang, M. Qiu, T. Ye, and Y. Su, "A tunable broadband photonic RF phase shifter based on a silicon microring resonator," *IEEE Photon. Technol. Lett.*, vol. 21, no. 1, pp. 60–62, Jan. 2009.
- [16] X. Liu *et al.*, "Broadband tunable microwave photonic phase shifter with low RF power variation in a high-Q AlN microring," *Opt. Lett.*, vol. 41, pp. 3599–3602, Aug. 2016.
- [17] R. Soref and B. Bennett, "Electrooptical effects in silicon," *IEEE J. Quantum Electron.*, vol. 23, no. 1, pp. 123–129, Jan. 1987.
- [18] D. Mishra and R. K. Sonkar, "Analysis of germanium-doped silicon vertical PN junction optical phase shifter," *J. Opt. Soc. Am. B*, vol. 36, pp. 1348–1354, May 2019.
- [19] C. Porzi *et al.*, "Photonic integrated microwave phase shifter up to the mm-wave band with fast response time in silicon-on-insulator technology," *J. Lightw. Technol.*, vol. 36, no. 19, pp. 4494–4500, Oct. 2018.
- [20] B. J. Eggleton, C. G. Poulton, P. T. Rakich, M. J. Steel, and G. Bahl, "Brillouin integrated photonics," *Nature Photon.*, vol. 13, no. 10, pp. 664–677, 2019.
- [21] R. W. Boyd, *Nonlinear Optics*, 3rd ed., New York, NY, USA: Academic, 2008.
- [22] M. Merklein, B. Stiller, and B. J. Eggleton, "Brillouin-based light storage and delay techniques," *J. Opt.*, vol. 20, Jul. 2018, Art. no. 083003.
- [23] M. Pagani, D. Marpaung, and B. J. Eggleton, "Ultra-wideband microwave photonic phase shifter with configurable amplitude response," *Opt. Lett.*, vol. 39, pp. 5854–5857, Oct. 2014.
- [24] M. Pagani, D. Marpaung, D.-Y. Choi, S. J. Madden, B. Luther-Davies, and B. J. Eggleton, "Tunable wideband microwave photonic phase shifter using on-chip stimulated Brillouin scattering," *Opt. Express*, vol. 22, pp. 28810–28818, Nov. 2014.
- [25] L. McKay *et al.*, "Brillouin-based phase shifter in a silicon waveguide," *Optica*, vol. 6, pp. 907–913, Jul. 2019.
- [26] E. A. Kittlaus, H. Shin, and P. T. Rakich, "Large Brillouin amplification in silicon," *Nature Photon.*, vol. 10, pp. 463–467, Jun. 2016.
- [27] A. H. Safavi-Naeini, D. V. Thourhout, R. Baets, and R. V. Laer, "Controlling phonons and photons at the wavelength scale: Integrated photonics meets integrated phononics," *Optica*, vol. 6, pp. 213–232, Feb. 2019.
- [28] M. Merklein *et al.*, "Stimulated Brillouin scattering in photonic integrated circuits: Novel applications and devices," *IEEE J. Sel. Topics Quantum Electron.*, vol. 22, no. 2, pp. 336–346, Mar./Apr. 2016.
- [29] D. C. Hutchings, M. Sheik-Bahae, D. J. Hagan, and E. W. Van Stryland, "Kramers-krönig relations in nonlinear optics," *Opt. Quantum Electron.*, vol. 24, pp. 1–30, Jan. 1992.
- [30] G. P. Agrawal, "Chapter 9 - Stimulated Brillouin scattering," in *Nonlinear Fiber Optics*, G. P. Agrawal, Ed., *Optics and Photonics*. 4th ed., San Diego, CA, USA: Academic Press, 2006, pp. 329–367.
- [31] B. J. Eggleton, C. G. Poulton, and R. Pant, "Inducing and harnessing stimulated Brillouin scattering in photonic integrated circuits," *Adv. Opt. Photon.*, vol. 5, pp. 536–587, Dec. 2013.
- [32] A. Choudhary *et al.*, "Linearity and resolution of on-chip Brillouin filters for rf and optical communications," in *Proc. Opto-Electron. Commun. Conf. and Photon. Global Conf.*, Jul. 2017, pp. 1–2.
- [33] I. Aryanfar *et al.*, "Chip-based Brillouin radio frequency photonic phase shifter and wideband time delay," *Opt. Lett.*, vol. 42, pp. 1313–1316, Apr. 2017.
- [34] M. B. Ayun, A. Schwarzbaum, S. Rosenberg, M. Pinchas, and S. Sternklar, "Photonic radio frequency phase-shift amplification by radio frequency interferometry," *Opt. Lett.*, vol. 40, pp. 4863–4866, Nov. 2015.
- [35] Y. Liu, A. Choudhary, D. Marpaung, and B. J. Eggleton, "Gigahertz optical tuning of an on-chip radio frequency photonic delay line," *Optica*, vol. 4, pp. 418–423, Apr. 2017.
- [36] A. Choudhary *et al.*, "High-resolution, on-chip RF photonic signal processor using Brillouin gain shaping and RF interference," *Scientific Rep.*, vol. 7, Jul. 2017, Art. no. 5932.
- [37] N. Zhang, X. Fu, J. Liu, and C. Shu, "Surpassing the tuning speed limit of slow-light-based tunable optical delay via four-wave mixing bragg scattering," *Opt. Lett.*, vol. 43, pp. 4212–4215, Sep. 2018.
- [38] A. Zarifi *et al.*, "Highly localized distributed Brillouin scattering response in a photonic integrated circuit," *APL Photon.*, vol. 3, Mar. 2018, Art. no. 036101.
- [39] A. Zarifi *et al.*, "Brillouin spectroscopy of a hybrid silicon-chalcogenide waveguide with geometrical variations," *Opt. Lett.*, vol. 43, pp. 3493–3496, Aug. 2018.
- [40] A. Zarifi *et al.*, "On-chip correlation-based Brillouin sensing: design, experiment, and simulation," *J. Opt. Soc. Am. B*, vol. 36, pp. 146–152, Jan. 2019.